Received: 26 November 2019 | Revised: 6 June 2020 | Accepted: 7 June 2020

DOI: 10.1111/jace.17319

ORIGINAL ARTICLE

Journal of the American Ceramic Society

Thermophysical properties and cyclic lifetime of plasma sprayed $SrAl_{12}O_{19}$ for thermal barrier coating applications

Xin Zhou[1,3] | **Wenjia Song**[2,3] | **Jieyan Yuan**[1,3] | **Qingmei Gong**[1] | **Hao Zhang**[1] | **Xueqiang Cao**[1] | **Donald B. Dingwell**[3]

[1]State Key Laboratory of Silicate Materials for Architectures, Wuhan University of Technology, Wuhan, China

[2]Department of Materials Science and Engineering, Beihang University, Beijing, China

[3]Department of Earth and Environmental Sciences, Ludwig-Maximilians-Universität (LMU) Münich, Munich, Germany

Correspondence
Wenjia Song, Department of Earth and Environmental Sciences, Ludwig-Maximilians-Universität (LMU), Theresienstrasse 41, 80333 Munich, Germany.
Email: wenjia.song@lmu.de

Xueqiang Cao, State Key Laboratory of Silicate Materials for Architectures, Wuhan University of Technology, Wuhan 430070, China.
Email: xcao@whut.edu.cn

Funding information
National Natural Science Foundation of China, Grant/Award Number: 51702244

Abstract

About 6-8 wt% yttria-stabilized zirconia (YSZ) is the industry standard material for thermal barrier coatings (TBC). However, it cannot meet the long-term requirements for advanced engines due to the phase transformation and sintering issues above 1200°C. In this study, we have developed a magnetoplumbite-type $SrAl_{12}O_{19}$ coating fabricated by atmospheric plasma spray, which shows potential capability to be operated above 1200°C. $SrAl_{12}O_{19}$ coating exhibits large concentrations of cracks and pores (~26% porosity) after 1000 hours heat treatment at 1300°C, while the total porosity of YSZ coatings progressively decreases from the initial value of ~18% to ~5%. Due to the contribution of porous microstructure, an ultralow thermal conductivity (~1.36 W m^{-1} K^{-1}) can be maintained for $SrAl_{12}O_{19}$ coating even after 1000 hours aging at 1300°C, which is far lower than that of the YSZ coating (~1.98 W m^{-1} K^{-1}). In thermal cyclic fatigue test, the $SrAl_{12}O_{19}$/YSZ double-ceramic-layer coating undertakes a thermal cycling lifetime of ~512 cycles, which is not only much longer than its single-layer counterpart (~163 cycles), but also superior to that of YSZ coating (~392 cycles). These preliminary results suggest that $SrAl_{12}O_{19}$ might be a promising alternative TBC material to YSZ for applications above 1200°C.

KEYWORDS

sintering resistance, $SrAl_{12}O_{19}$, thermal barrier coatings, thermal conductivity, thermal cycling

1 | INTRODUCTION

The demand for more powerful and efficient gas turbine engines has accelerated the development of advanced materials to enable the increasing engine operating temperature.[1-3] Due to their excellent high-temperature stability and low-density, Si-based ceramic matrix composites (CMCs) are currently considered as an attractive alternative for replacing Ni-based superalloys in the next generation gas turbines.[2] However, both the currently used superalloys and CMCs for further designs of advanced gas turbines rely on ceramic coatings to protect them from the harsh combustion environments.[2] Currently, thermal barrier coatings (TBC) have been widely developed to provide thermal insulation to the superalloy engine parts,[3,4] while environmental barrier coatings (EBC) are developed for CMCs to prevent them from reacting with water vapor.[5-7] In more aggressive designs, an additional TBC top coat will be deposited on CMCs to build thermal/environmental barrier coatings (T/EBC) for even higher temperature applications.[2,8-13] About 6-8 wt% yttria partially stabilized zirconia (YSZ), which is the current industry standard TBC material, becomes challenged in such advanced TBC and T/EBC systems due to its limited temperature capability.[14,15] At temperatures higher than 1200°C, it undergoes a martensitic phase transformation from the initial *t´*-tetragonal zirconia to the final monoclinic (*m*) zirconia, which brings

with significant detrimental effects on the durability of the TBCs.[16-18] Furthermore, the accelerated sintering of YSZ coatings above 1200°C generally results in higher Young's modulus and thermal conductivity, leading to a reduction of strain tolerance and thermal insulation.[19]

To meet the requirement of further ultraefficient propulsion engine systems, the search for new materials that can withstand higher gas-inlet temperature has been intensified in the last few decades.[20] Refractory oxides such as rare-earth zirconates ($R_2Zr_2O_7$, R = La, Nd, Sm, Gd),[21-26] rare-earth hafnates ($La_2Hf_2O_7$,[27,28] $Yb_3Hf_4O_{12}$[29,30]), $Y_3Zr_4O_{12}$,[31] and $LaMgAl_{11}O_{19}$[32] have been proposed as new T/EBC candidates. In particular, MgO-doped rare-earth hexaluminates $RMgAl_{11}O_{19}$ (RMA) with a magnetoplumbite structure have attracted increasing attention due to their promising thermophysical properties and excellent thermal stability up to 1800°C.[33] Such oxides were also found to possess high fracture toughness and outstanding sintering resistance, which is mainly attributed to their platelet-like grains with high aspect ratio.[33-36] In our former experiment, we found that a plasma sprayed LMA coating had a lifetime more than 11 000 cycles at the surface testing temperature of 1250°C, comparable to that of YSZ coating. At 1350°C, the thermal shock lifetime of LMA/YSZ functionally graded TBC system was found to be ~8 times as long as that of YSZ coating.[37] LMA coatings also can provide good thermal insulation and oxidation protection for CMCs.[38] However, there are two critical factors hindering their extensive application. One of these is the deposition of nonstoichiometric phases during plasma spraying. Loss of MgO in LMA coating due to its extremely high vapor pressure (ie, volatility) has already been reported on Ref. [39] It leads to an impurity phase that might be detrimental to the coating performance. In addition, RMA has exhibited poor stability with significant weight loss at temperatures above 1500°C in a water-bearing atmosphere.[40] This has been attributed to H^+/Mg^{2+} ionic exchange, which leads to Mg^{2+} migration from the intrinsic site in the RMA crystal structure.[41] Thus, it would appear that the development of MgO-free hexaluminates might be an effective strategy to improve the coating heterogeneity and environmental durability.

Two types of MgO-free hexaluminates including rare-earth hexaluminates $RAl_{11}O_{18}$ (R = La, Nd, Sm) and alkaline earth hexaluminates $AAl_{12}O_{19}$ (A = Ca, Sr, Ba) have been investigated for potential TBC applications (Figure S1-S5, the detailed information can be found in supplementary material). The results clearly demonstrate that $SrAl_{12}O_{19}$ has the best combination of properties among all the hexaluminates examined. The objective of this study is to investigate the performance of $SrAl_{12}O_{19}$ as a novel TBC material. Phase stability, sintering, and thermal conductivity of plasma sprayed $SrAl_{12}O_{19}$ coatings were evaluated and compared with YSZ coatings. The thermal cycling durability of $SrAl_{12}O_{19}$-based TBCs were investigated by furnace cyclic testing and the associated failure mechanism was also discussed.

2 | EXPERIMENTAL PROCEDURE

2.1 | Materials

$SrAl_{12}O_{19}$ powders were synthesized by the traditional solid-state reaction with $SrCO_3$ (AR, Beijing Chemical Works) and γ-Al_2O_3 (99.99%, Tangshan Huatai Functional Ceramic Materials Co., Ltd.) as the starting materials. The appropriate amounts of individual oxides were mechanically milled for 24 hours, and then, were calcined at 1400°C for 6 hours. The as-synthesized $SrAl_{12}O_{19}$ powders were spray-dried and sieved size fractions of 25-125 μm were used. $SrAl_{12}O_{19}$ coatings were produced by using a Multicoat Plasma Spray Unit (Oerlikon Metco, Switzerland) and the APS parameters are listed in Table 1. Free-standing $SrAl_{12}O_{19}$ coatings were sprayed onto a graphite substrate, which was subsequently removed by oxidation at 700°C in air. For thermal cycling, $SrAl_{12}O_{19}$ coatings were sprayed on DZ125 superalloy substrates coated with a ~80 μm NiCrAlY bond coat. The deposition parameters for bond coat are also listed in Table 1. In addition, YSZ, LMA, and $Gd_2Zr_2O_7$-based TBCs were also produced based on the identical APS parameter (as listed in Table 1) for comparison with $SrAl_{12}O_{19}$ coatings.

2.2 | Thermal exposure

To study the phase stability and sintering resistance of the plasma sprayed coatings, the 10 mm × 10 mm × 1 mm $SrAl_{12}O_{19}$ and YSZ free-standing coatings were isothermally aged at 1300°C for a prescribed dwell time (40-1000 hours).

TABLE 1 Main plasma spraying parameters

Coatings	Power (kW)	Distance (mm)	Plasma gas Ar/H_2 (slpm)	Feeding rate (g/min)
Bond coat	42	100	35/12	30
Top coat	42	100	35/12	35

Abbreviation: slpm, standard liter per minute.

Thermal cycling tests of the coating samples were performed using a vertical furnace which is equipped with an automation system allowing specimens moving in and out automatically. In the thermal cycling test experiments, samples were heated in the air furnace at 1100°C for 50 minutes followed by removing out for cooling with airflow for 10 minutes. This process was stopped when 10% of the area of the ceramic coating was delaminated, and the number of the cycles was defined as the lifetime of the TBCs.

2.3 | Characterizations

Phase compositions and crystal structure were confirmed by X-ray diffraction (XRD, Rotation Anode High Power X-ray Diffractometer, CuKα radiation, $\lambda = 0.15406$ nm) in a detective range of $2\theta = 20°$~$80°$. Field emission scanning electron microscope (FE-SEM, QUANTA FEG 450) instrument equipped with an energy dispersive X-ray spectrum (EDS) was performed to determine the morphology, microstructure, and compositions of the coating. Prior to such sample inspection, it is necessary to sputter a thin Pt layer on the surface to upgrade electrical conductivity. The coating for cross-section analysis was mounted in transparent epoxy resin and polished finely with diamond pastes. The porosity of the coating was determined by image analysis using the back-scattered SEM images. More than five photos (500× magnification) randomly taken on the polished cross sections were used to measure the porosity. Globular pores and microcracks were separated and analyzed by using Image J software. The microcracks with an orientation between 45° and 135° were defined as vertical microcracks, whereas microcracks between 0° and 45° and between 135° and 180° were defined as lateral microcracks. Microcracks including vertical microcracks and lateral microcracks were skeletonized and counted in terms of length according to the above definition. Other details could be found in Ref. [42] To determine quantitatively the chemical compositions of the as-sprayed $SrAl_{12}O_{19}$ coating, a prototype field emission electron probe microanalyzer (FE-EPMA) was also employed.

The coefficients of thermal expansion (CTE) were determined from room temperature to 1500°C with a high-temperature dilatometer (NETZSCH DIL 402C, Germany). The specimen used for CTE measurements was fabricated to the dimensions of ~27 mm × 4 mm × 1 mm. The thermal diffusivity was measured using a laser flash technique (LFA457, Germany). The surfaces of the samples (~10 mm × 10 mm × 1 mm) were covered with a thin film of graphite for thermal absorption producing by laser pulses prior to thermal diffusivity measurements. The density of the as-sprayed and annealed coatings was determined by measuring their mass and volume using an electronic analytical balance and a micrometer, respectively. Heat-capacity measurements were performed using a NETZSCH STA 449 F3 Jupiter simultaneous thermal analyzer. The specific heat capacity of the annealed YSZ and $SrAl_{12}O_{19}$ coatings was calculated relatively to the specific heat capacity of the sapphire reference sample. The thermal conductivity (k) was further calculated using the following equation:[43,44]

$$k = C_p \cdot \rho \cdot \lambda, \tag{1}$$

where C_p is the specific heat capacity; ρ is the density; and λ is the thermal diffusivity.

3 | RESULTS AND DISCUSSION

3.1 | Characteristics of as-sprayed $SrAl_{12}O_{19}$ coating

As $SrAl_{12}O_{19}$ has the most promising combination of properties relative to TBC applications among binary hexaluminates, $SrAl_{12}O_{19}$ coatings were deposited by plasma spray and preliminary evaluation of $SrAl_{12}O_{19}$ as TBC material is further developed below.

The typical morphology of the as-sprayed $SrAl_{12}O_{19}$ coating is shown in Figure 1. It has a rough surface where partially melted ceramic powders and the lamellae zones coexist (Figure 1A,B). The cross-sectional SEM image of $SrAl_{12}O_{19}$ coating (shown in Figure 1C) exhibits a porous structure. The average thickness of the $SrAl_{12}O_{19}$ coating is measured to ~240 μm and the adhesion of the coating to bond coat seems to be excellent. In order to identify the coating composition and homogeneity, EPMA analysis was conducted by randomly selecting five points along the cross section. The result presented in Figure 1D shows atom ratio of Al:Sr is about 12, indicating the $SrAl_{12}O_{19}$ coating with nearly stoichiometric composition was successfully produced by plasma spraying. The XRD pattern of the as-sprayed $SrAl_{12}O_{19}$ coating is given in Figure 1E. Characteristic peaks of the magnetoplumbite structure can be identified in the XRD pattern. Compared with the XRD pattern of $SrAl_{12}O_{19}$ powder (Figure S1B), the as-sprayed coating contains ~ 42% amorphous index due to the quenching of the molten droplets from the plasma flame to the substrate during the APS process.[39,43]

3.2 | Phase stability of $SrAl_{12}O_{19}$ coating

To study the phase stability of the $SrAl_{12}O_{19}$ coating, the free-standing coatings were exposed to long-term annealing at 1300°C and XRD analysis of the annealing products was conducted. As shown in Figure 2A, the crystallization has almost completed after heat-treated for 5 hours at 1300°C.

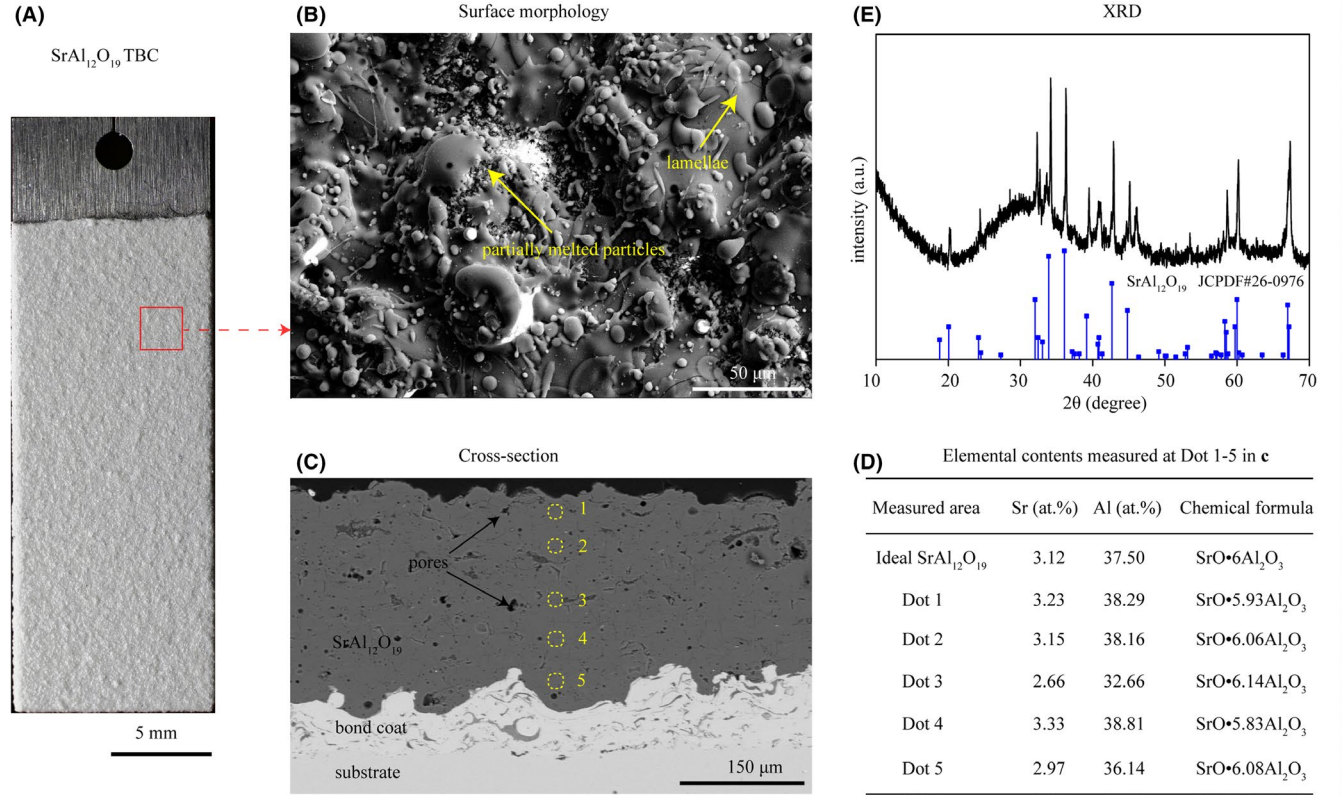

(D) Elemental contents measured at Dot 1-5 in **c**

Measured area	Sr (at.%)	Al (at.%)	Chemical formula
Ideal $SrAl_{12}O_{19}$	3.12	37.50	$SrO{\bullet}6Al_2O_3$
Dot 1	3.23	38.29	$SrO{\bullet}5.93Al_2O_3$
Dot 2	3.15	38.16	$SrO{\bullet}6.06Al_2O_3$
Dot 3	2.66	32.66	$SrO{\bullet}6.14Al_2O_3$
Dot 4	3.33	38.81	$SrO{\bullet}5.83Al_2O_3$
Dot 5	2.97	36.14	$SrO{\bullet}6.08Al_2O_3$

FIGURE 1 Morphology and composition of the as-sprayed $SrAl_{12}O_{19}$ coating. A, Surface photo; B, Surface microstructure; C, Polished cross-sectional morphology; D, EPMA results of the five areas in Figure 4C; E, XRD result obtained from the coating surface

It is found that the 40 hours annealed coating has the ideal magnetoplumbite structure. After annealing at 1300°C for 1000 hours, no difference among the XRD patterns can be observed, indicating that the $SrAl_{12}O_{19}$ coating is thermally stable in the temperature range of interest for TBC applications.

3.3 | Sintering resistance of $SrAl_{12}O_{19}$ coating

During service, long-term high-temperature exposure often leads to inevitable sintering of the ceramic coating, which has significant detrimental effect on the performance of TBC.[45-47] In order to evaluate the sintering resistance, microstructural evolution of $SrAl_{12}O_{19}$ coating and YSZ coating during heat-treatment was investigated and compared. As shown in Figure 3A, different types of pores can be observed in the as-sprayed YSZ coating, including spherical or nearly spherical three-dimensional pores (globular pores), inter-splat pores (defined as horizontal microcracks in Table 2), and inter-splat cracks (defined as vertical microcracks in Table 2). The total porosity of the as-sprayed YSZ coating is estimated to be ~17.89%, which consists of ~8.08% globular porosity, ~7.55% inter-splat pores and ~2.26% inter-splat cracks (as listed in Table 2). After 40 hours thermal exposure at 1300°C, the formation of sintering necks occurred between the splats and microcracks (Figure 3B). The inter-splat pores, inter-splat cracks, and small globular pores reduce rapidly, resulting in approximately 54% drop in the total porosity (as listed in Table 2). After a longer thermal exposure (>40 hours), pores and cracks heal slowly and the large pores become shallower and more globular. The total evolution can be approximately divided into two stages. In the stage Ⅰ (0-40 hours), the porosity of YSZ coating decreased rapidly which can be attributed to the healing of microcracks and small pores through multipoint connections (Figure 3C).[48-50] During stage Ⅱ (40-1000 hours), the relatively wider pores and cracks decreased the possibility of multipoint connection, so the sintering speed is significantly lower. At the end of the annealing test (1000 hours), most of the microcracks and small pores cannot be observed and only large voids remained in YSZ coatings, resulting in a final porosity of about 5%.

As shown in Figure 4A, the lamellar structure as found in the APS YSZ coating is absent for the as-sprayed $SrAl_{12}O_{19}$ coating. Only globular pores and a small amount of microcracks can be observed for the as-sprayed $SrAl_{12}O_{19}$ coating and the total porosity is estimated to be ~18.05%. After

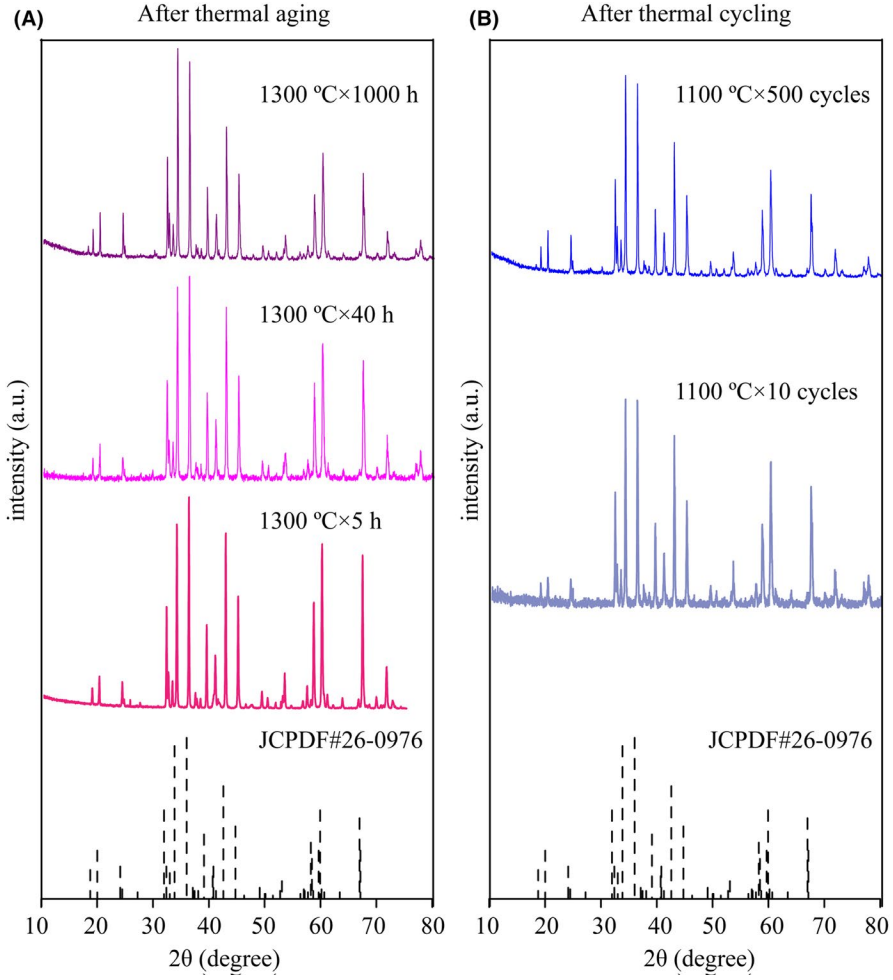

FIGURE 2 XRD of the $SrAl_{12}O_{19}$ coatings: A, After thermal aging at 1300°C; B, After thermal cycling at 1100°C

40 hours thermal exposure at 1300°C, we note that a high concentration of plate-like grains with high aspect ratios seem to be recrystallized in situ from the molten lamellae of the coatings (Figure 4C). The randomly arranged platelet-like hexagonal grains lend $SrAl_{12}O_{19}$ coating a higher porosity (~23.21%, as listed in Table 3). Comparing the microstructure with that of the as-sprayed $SrAl_{12}O_{19}$ coating, it is possible to find obvious increase of microcracks, without a significant change in the amounts of globular pores. In the following extended thermal exposure stage (40-1000 hours), the $SrAl_{12}O_{19}$ coatings show an increase in microcracks due to the crack propagation, and a drop in globular porosity due to the sintering effect. It should be noted that the increase in microcracks is much more pronounced than the decrease of the globular porosity. Consequently, the total porosity of the $SrAl_{12}O_{19}$ coatings increases slightly. The $SrAl_{12}O_{19}$ coating still contains large concentrations of porosity even after 1000 hours heat treatment at 1300°C (Table 3). The high sintering resistance of $SrAl_{12}O_{19}$ coating may be attributed to an increase of the total volume of the microcracks and the random stacking of the platelet-like crystals. A low sintering rate is highly advantageous in TBC applications, helping to maintain the original porous structure of TBC, thus, giving rise to a high strain tolerance and good thermal insulating efficiency.[47]

3.4 | Evolution of thermal conductivity during thermal exposure

Figure 5 compares the thermal properties changes in $SrAl_{12}O_{19}$ and YSZ free-standing coatings. It can be observed that both the thermal diffusivities of $SrAl_{12}O_{19}$ and YSZ coatings decrease gradually with temperature, consistent with the phonon conduction mechanism being dominant for these coatings. The significant increase of thermal diffusivities with aging time is observed in YSZ coatings (Figure 5A), which is primarily attributed to the sharp decrease in porosity as discussed above. For $SrAl_{12}O_{19}$ coatings, the thermal diffusivities initially increase with aging, followed by a slight decrease from 100 to 1000 hours (Figure 5B).

The middle of Figure 5A,B show the results of specific heat capacity (C_p) measurements for YSZ and $SrAl_{12}O_{19}$ coatings. For the as-sprayed YSZ coating, the specific heat capacity increases gradually from 0.458 to 0.634 J/g·K in the temperature range between 25°C and

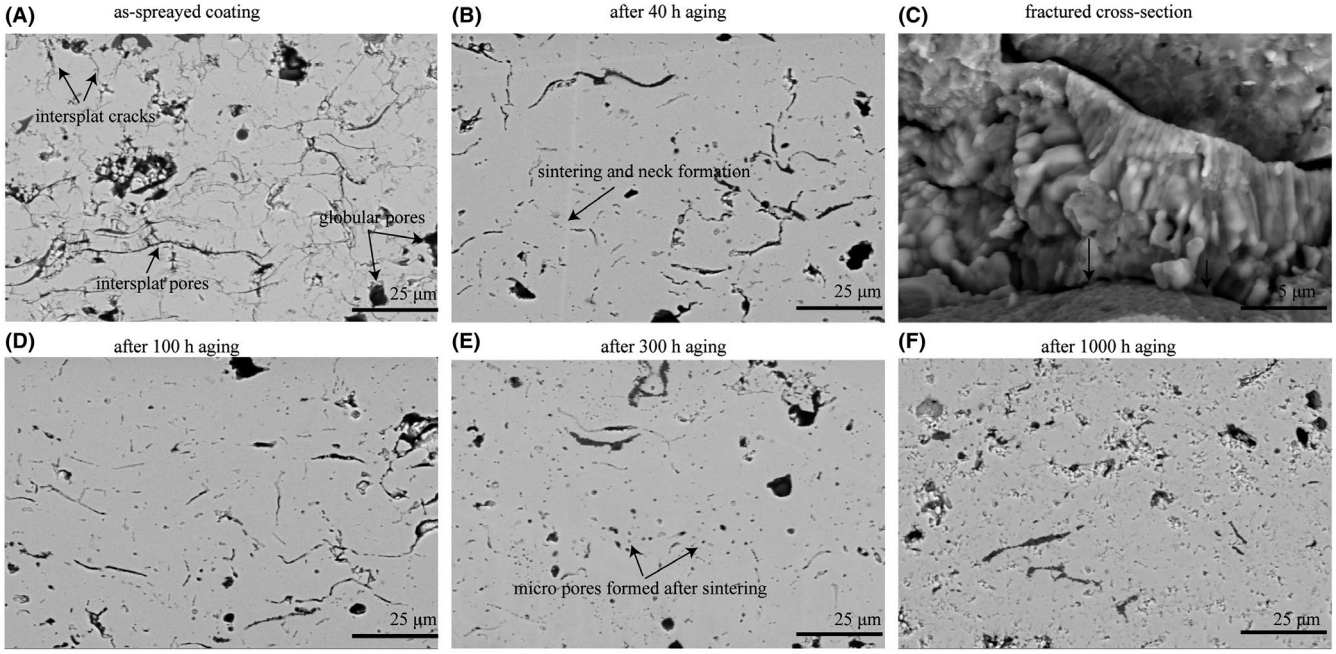

FIGURE 3 Microstructural evolution of YSZ coatings during aging at 1300°C. A, As sprayed; B, 40 h; D, 100 h; E, 300 h; F, 1000 h; C, fractured cross section of YSZ coating after 40 h aging

TABLE 2 Statistical results of different types of pore for the as-sprayed and heat-treated YSZ coatings

Aging time (h)	Total porosity (%)	Globular porosity (%)	Horizontal microcracks (%)	Vertical microcracks (%)
0	17.89 ± 1.07	8.08 ± 1.75	7.55 ± 0.83	2.26 ± 0.63
40	8.28 ± 0.80	5.42 ± 1.28	2.11 ± 0.69	0.75 ± 0.25
100	7.70 ± 0.75	5.25 ± 0.89	1.70 ± 0.54	0.74 ± 0.28
300	7.29 ± 0.42	5.24 ± 0.87	1.69 ± 0.40	0.35 ± 0.21
1000	5.26 ± 0.43	5.26 ± 0.43	—	—

1000°C. After 40 hours thermal exposure at 1300°C, the C_p of YSZ coating shows a slight increase, consistent with the results reported by Girolamo et al[51] The possible reason is due to the sintering of the porous microstructure and the decomposition of the metastable *t*' phase.[51] For as-sprayed $SrAl_{12}O_{19}$ coating, C_p is around 0.629 J/g·K at 25°C and 1.043 J/g·K at 1000°C. Unlike YSZ coatings, C_p of $SrAl_{12}O_{19}$ coatings decreases for the thermal aged coatings, which may be associated with the increase of coating porosity and the crystallization of the amorphous phase during aging. The different evolution of C_p for these two coatings could be explained by their different sintering behavior. It should be noted that the aging time seems not to significantly influence the heat capacity of the YSZ and $SrAl_{12}O_{19}$ coatings after 40-1000 hours exposure due to their very close microstructure and phase composition.

The thermal conductivity of $SrAl_{12}O_{19}$ and YSZ coatings were calculated by Equation (1), using the data of Figure 5 and Table 4. As shown in Figure 5B, the thermal conductivities of as-sprayed $SrAl_{12}O_{19}$ coatings are in a range of 1.00-1.22 W m^{-1} K^{-1}. It is apparent that the thermal conductivity of the as-sprayed $SrAl_{12}O_{19}$ coating is well below that of the bulk material (Figure S6), which is not only resulted from the pores and cracks in the APS structure, but also from the large amount of amorphous phase presented in the as-sprayed $SrAl_{12}O_{19}$ coating. Compared to the conventional YSZ coatings, the $SrAl_{12}O_{19}$ coatings show a relatively higher thermal conductivity in the as-sprayed state, but they exhibit a much lower degradation rate in thermal conductivity during heat treatment.

Figure 6A represents the thermal conductivities of the aged YSZ and $SrAl_{12}O_{19}$ coatings at 1000°C, which is a temperature relevant for TBC applications. As shown in Figure 6A, the thermal conductivity of YSZ coatings increases from 0.78 to 1.98 W m^{-1} K^{-1} when the aging time increases from 0 to 1000 hours. The total evolution can be separated into two stages, termed as stage Ⅰ and stage Ⅱ. The greatest increase of thermal conductivity occurs within stage Ⅰ (0-40 hours) presumably due to the porosity

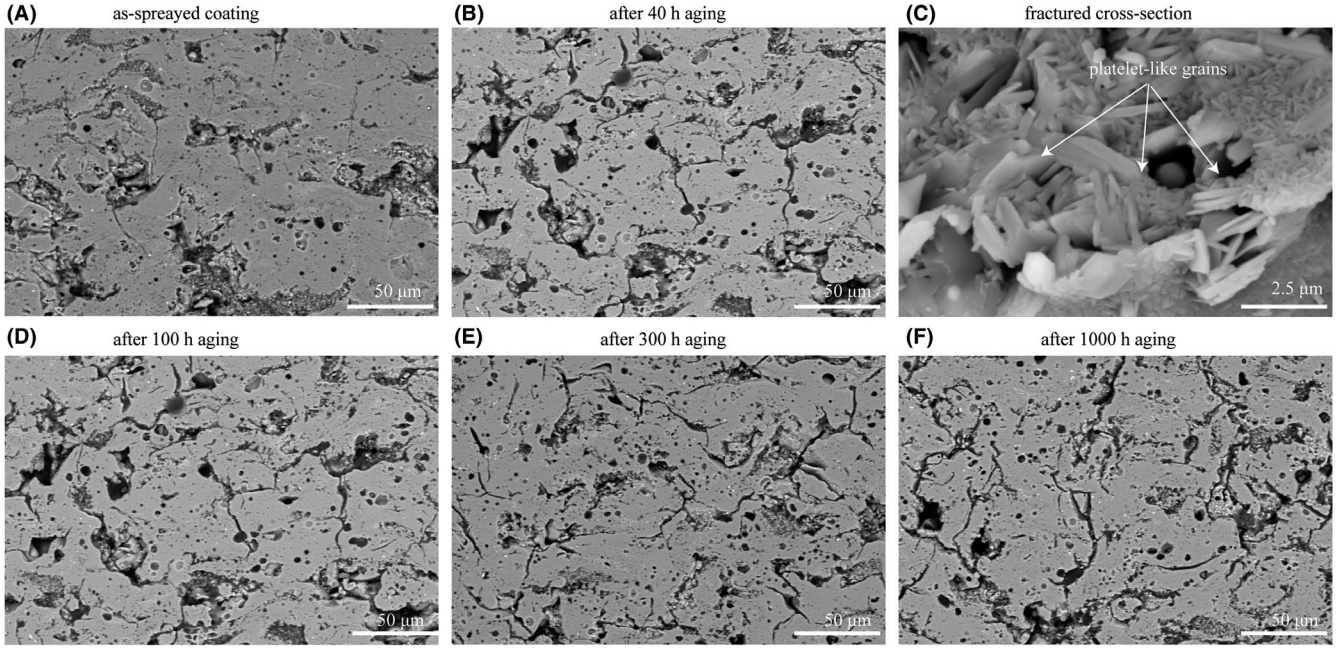

FIGURE 4 Microstructural evolution of the $SrAl_{12}O_{19}$ coatings during aging at 1300°C. A, As sprayed; B, 40 h; D, 100 h; E, 300 h; F, 1000 h; C, fractured cross section of $SrAl_{12}O_{19}$ coating after 40 h aging

TABLE 3 Statistical results of different types of pore for the as-sprayed and heat-treated $SrAl_{12}O_{19}$ coatings

Aging time (h)	Total porosity (%)	Globular porosity (%)	Microcracks (%)
0	18.05 ± 3.74	16.06 ± 3.15	1.99 ± 0.78
40	23.21 ± 3.27	15.55 ± 2.42	7.66 ± 1.57
100	24.73 ± 1.23	15.33 ± 2.06	9.40 ± 1.66
300	25.53 ± 3.64	15.29 ± 1.95	10.24 ± 2.03
1000	26.14 ± 1.80	15.16 ± 1.18	10.98 ± 1.92

reduction caused by intense sintering of inter-splat pores, inter-splat cracks, and small globular pores in YSZ coatings (Figure 3). In stage II (100-1000 hours), the rate of thermal conductivity changes flatters off with increased duration, correlating to the slow sintering rate from 100 to 1000 hours (Table 2). For $SrAl_{12}O_{19}$ coatings, the trend of thermal conductivity changes also can be divided into two stages (Figure 6A). During the first 100 hours heat treatment at 1300°C, the thermal conductivity of $SrAl_{12}O_{19}$ coatings increases from 1.22 to 1.42 W m^{-1} K^{-1}, after that it decreases slightly and reaches to 1.36 W m^{-1} K^{-1} after 1000 hours aging, which is much different from that of YSZ coatings. As mentioned above, the porosity of $SrAl_{12}O_{19}$ coatings increases as aging time goes longer, which implies that the increase of thermal conductivity in stage I cannot be attributed to coating porosity reduction as that found in YSZ coating. For a certain chemical composition of solid material, their amorphous state exhibits a much lower thermal conductivity than any other crystalline state.[47] Therefore, we postulate that the reduction of amorphous phase during heat treatment is responsible for the initial increase of thermal conductivity in $SrAl_{12}O_{19}$ coatings. In stage II, crystallization of the $SrAl_{12}O_{19}$ coating is complete (Figure 2), after which the random stacking of the platelet-like grains of $SrAl_{12}O_{19}$ coating leading to a higher porosity could result in a slight reduction in thermal conductivity.

Figure 6B compares the increment of normalized thermal conductivities of the YSZ and $SrAl_{12}O_{19}$ coatings, which is defined as the ratio of a thermal conductivity increment to its corresponding initial value. The initial thermal conductivity of stage I and stage II is defined as the value at 0 and 100 hours, respectively. It can be seen that the increment of normalized thermal conductivity for YSZ and $SrAl_{12}O_{19}$ coatings are 115.6% and 14.4%, respectively, during stage I. The result clearly shows that $SrAl_{12}O_{19}$ coating has a much lower degradation rate in thermal insulation property in stage I. In stage II, the thermal conductivity of YSZ coating continues to increase, albeit more slowly. The increment of normalized thermal conductivity is about 8.6% in stage II. In contrast, there is a 4.2% decrease in normalized thermal conductivity for $SrAl_{12}O_{19}$ coatings, suggesting that the thermal insulation of $SrAl_{12}O_{19}$ coatings is recovered in stage II to some extent. Due to the extremely low sintering rate, a relatively low thermal conductivity could be maintained for $SrAl_{12}O_{19}$ coating even after long-term aging (1000 hours). The formation of cracks in $SrAl_{12}O_{19}$ coating during thermal exposure is seen to provide benefit for TBC applications by maintaining a low thermal

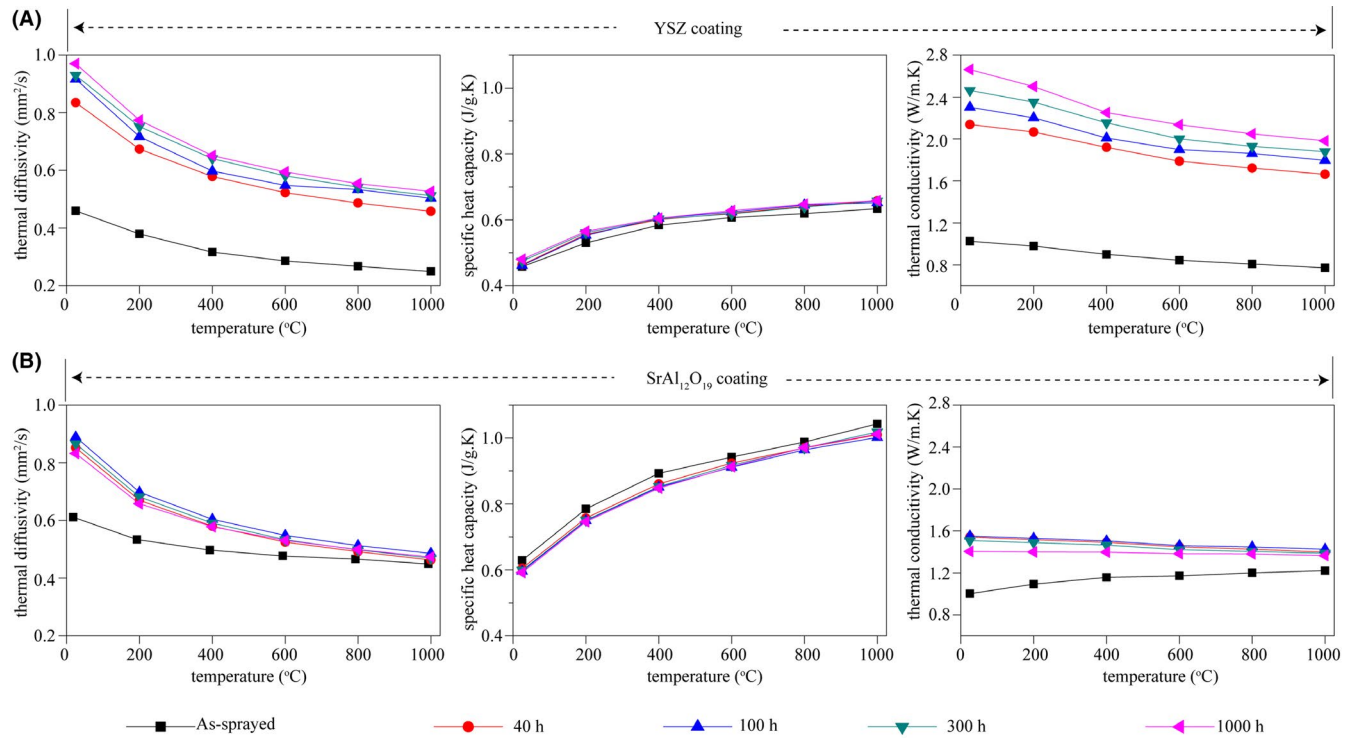

FIGURE 5 The evolution of thermal diffusivity, specific heat capacity, and thermal conductivity of the YSZ (A) and $SrAl_{12}O_{19}$ coatings (B) during aging at 1300°C

TABLE 4 Density of as-sprayed and heat-treated YSZ and $SrAl_{12}O_{19}$ coatings

Condition	Density (g/cm^3)	
	YSZ coating	$SrAl_{12}O_{19}$ coating
Theoretic value	6.04	4.02
As-sprayed	4.86	2.61
1300°C × 40 h	5.52	2.99
1300°C × 100 h	5.55	2.93
1300°C × 300 h	5.57	2.91
1300°C × 1000 h	5.72	2.85

conductivity. An undesirable effect, however, could be the reduction in mechanical properties. Further work is required to examine the influence of thermal exposure on the mechanical properties of $SrAl_{12}O_{19}$ coating.

3.5 | Thermal cycling durability of $SrAl_{12}O_{19}$-based TBCs

The thermal cycling durability of $SrAl_{12}O_{19}$ single-layer coating was evaluated by a thermal cyclic fatigue test at 1100°C. As shown in Figure 7A, spallation at the outer rim is observed after thermal cycling and the average lifetime is ~163 cycles. SEM micrograph of the failed $SrAl_{12}O_{19}$ coating (Figure 7B) shows that large horizontal cracks causing the coating spallation were formed in the $SrAl_{12}O_{19}$ coating very near to the bond coat/top coat interface. The average thickness of TGO is about 2 μm for the failed $SrAl_{12}O_{19}$ coating, which is far less than the critical value of 7-8 μm required to drive a complete delamination of the ceramic coating.[52] It is generally accepted that CTE mismatch between the ceramic coating and substrate is an important factor responsible for the thermal cyclic fatigue failure. Hence, CTE of $SrAl_{12}O_{19}$ coating before and after thermal aging at 1300°C for 40 hours was measured.

As illustrated in Figure 7C, CTE of the as-sprayed $SrAl_{12}O_{19}$ coating is much lower than that of the $SrAl_{12}O_{19}$ bulk due to large amount of amorphous phase within it. In addition, there is significant thermal contraction of ~1.9% at temperatures range from 869°C to 911°C, and a second shrinkage of ~0.6% at temperatures range from 1162°C to 1240°C. Based on the DSC curves (Figure S7), the two shrinkages may correspond to the recrystallization of amorphous $SrAl_{12}O_{19}$ coating. After aging at 1300°C for 40 h, $SrAl_{12}O_{19}$ coating shows a similar thermal expansion behavior to the $SrAl_{12}O_{19}$ bulk and the average CTE is measured to be ~7.52×10^{-6} K^{-1}. It should be noted that the recrystallization almost completed after 10 thermal cycles (Figure 2B). Therefore, CTE of the aged $SrAl_{12}O_{19}$ coating will be used in the following thermal stress evaluation.

Since $SrAl_{12}O_{19}$ coating showed no obvious phase transformation except the un-reversible amorphous crystallization (Figure 2), thermal cycling failure of the $SrAl_{12}O_{19}$ coating

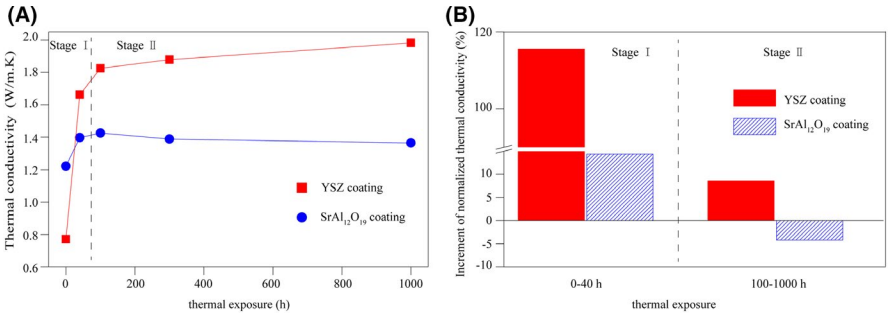

FIGURE 6 A, Thermal conductivities of the YSZ and $SrAl_{12}O_{19}$ coatings at 1000°C during aging; B, The increment of the normalized thermal conductivities in two stages

is interpreted to be mainly driven by the thermal expansion mismatch stress which can be expressed by the following equation[52]:

$$\sigma_0 \approx \frac{\Delta\alpha \cdot \Delta T \cdot E}{(1-\upsilon)}, \quad (2)$$

where σ_0 is the thermal stress, $\Delta\alpha$ is the CTE difference between the coating and the substrate, ΔT is the temperature difference, E and υ are the elastic modulus and Poisson ratio of the coating, respectively. The large CTE difference between $SrAl_{12}O_{19}$ coating (~7.52 × 10^{-6} K^{-1}) and MCrAlY bond coat (13-17 × 10^{-6} K^{-1})[25] could cause a large interface thermal stresses according to Equation (2). On the contrary, the formation of interface deficiencies due to the amorphous recrystallization would reduce the bond strength between $SrAl_{12}O_{19}$ coating and MCrAlY bond coat. When the interface stress accumulates to a critical level, horizontal cracks at the interface of $SrAl_{12}O_{19}$ coating and bond coat begin to form, propagate, and bridge, which finally cause $SrAl_{12}O_{19}$ coating spallation.

This shortcoming can be overcome by using a double-ceramic-layer (DCL) structure consisting of YSZ as a buffer layer between the bond coat and $SrAl_{12}O_{19}$ top coat (Figure 8A). The macroscopic patterns of the $SrAl_{12}O_{19}$/YSZ DCL coatings in different cycles are shown in Figure 8B. As compared to the corresponding single-layer TBC, a significant improvement in thermal cycling lifetime has been achieved for the $SrAl_{12}O_{19}$/YSZ DCL coatings. Figure 8C compares the cross-sectional microstructure before and after thermal cycling failure. It indicates that the failure of $SrAl_{12}O_{19}$/YSZ DCL coating always appears in YSZ layer close to the bond coat, whereas the interface between $SrAl_{12}O_{19}$ layer and YSZ layer is still intact, indicating that the stress concentration caused by thermal expansion mismatch between the $SrAl_{12}O_{19}$ coating and bond coat is eased by the presence of the YSZ buffer layer. Most of the DCL coatings reported in literature such as $La_2Zr_2O_7$/YSZ,[25] $Gd_2Zr_2O_7$/YSZ,[26] or $SrZrO_3$/YSZ[44] coatings showed a failure at the interface between the two ceramic layers, which has never been the case in the present study. A possible explanation for the difference in failure mode between $SrAl_{12}O_{19}$/YSZ coating and the $La_2Zr_2O_7$/YSZ coating could be the differences in their microstructure evolution and fracture toughness. Pyrochlores or perovskites has a lower fracture toughness compared to YSZ,[33] and hence, crack propagates faster in the new TBC layer of the DCL coatings. In contrast, $SrAl_{12}O_{19}$ has comparable fracture toughness to YSZ (Figure S4). It should

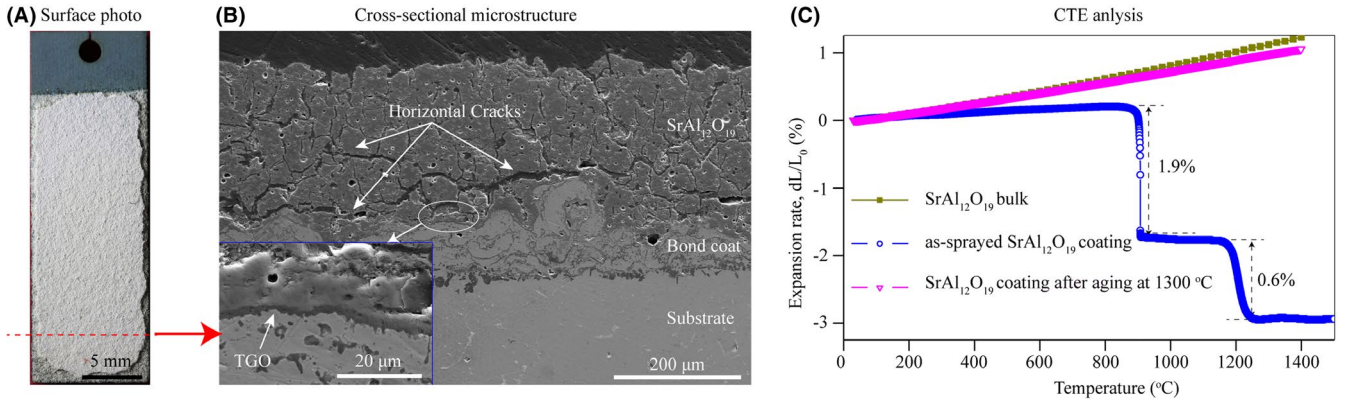

FIGURE 7 Thermal cycling behavior of $SrAl_{12}O_{19}$ coating at 1100°C. A, Macroscopic photograph of the failed $SrAl_{12}O_{19}$ coating. The dashed line shows the cutting direction of the sample for cross-sectional microstructure analysis; B, Cross-sectional SEM image of $SrAl_{12}O_{19}$ coating after thermal cycling. The inset image is the selected district with higher magnification; C, Linear thermal expansion curve of $SrAl_{12}O_{19}$ coating before and after thermal aging in comparison with the bulk of $SrAl_{12}O_{19}$

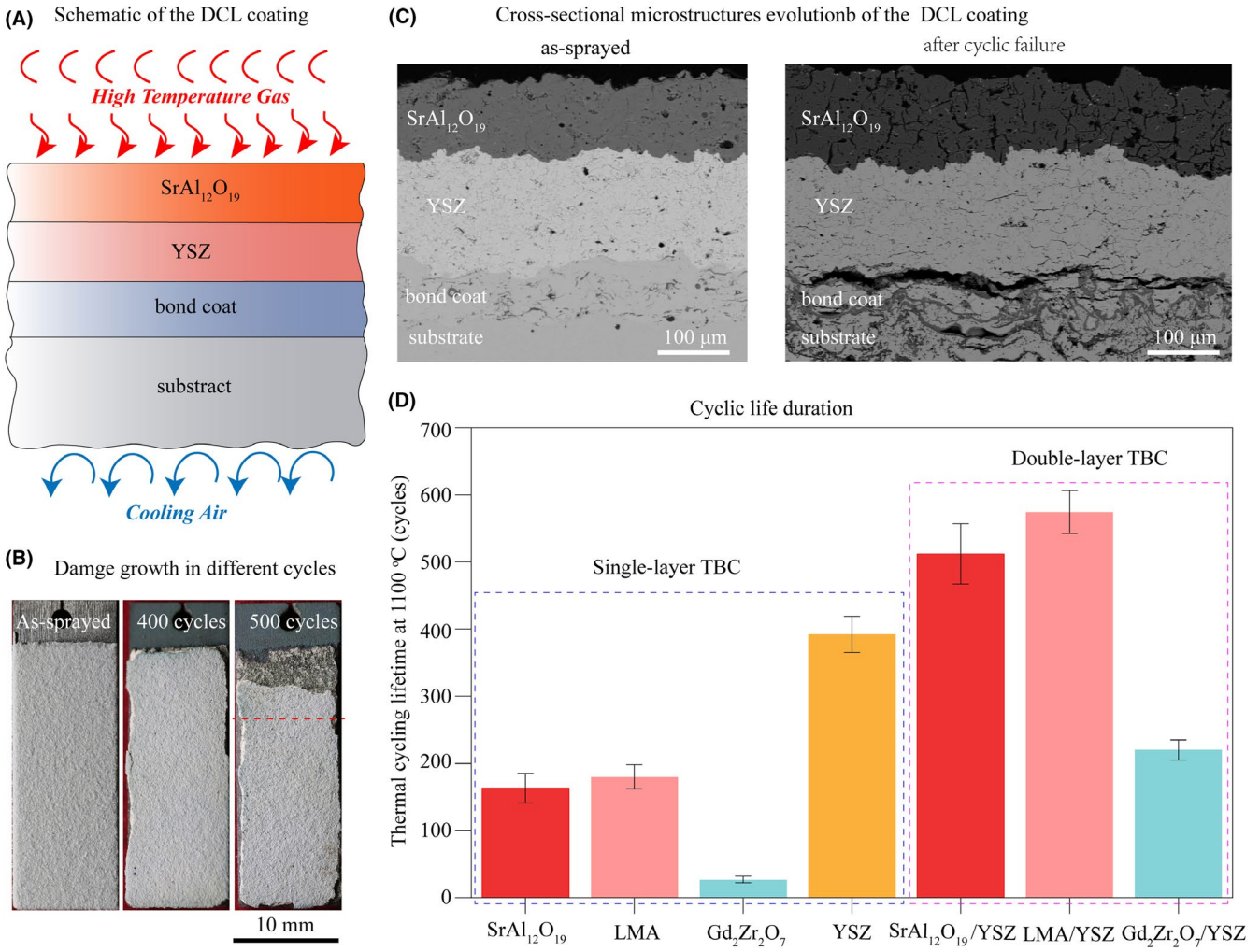

FIGURE 8 The preparation and failure of the $SrAl_{12}O_{19}$/YSZ DCL coating. A, Schematic illustration of $SrAl_{12}O_{19}$/YSZ DCL coating; B, Macroscopic photographs show the damage growth in different cycles; C, Cross-sectional SEM images of the $SrAl_{12}O_{19}$/YSZ coating before and after thermal cycling failure; D, Thermal cycling lifetime of different TBCs at 1100°C

be noted that there are a large number of microcracks in the $SrAl_{12}O_{19}$ coating after thermal cycling, and crack deflections commonly observed (Figure 8C). The vertical crack networks might impart the $SrAl_{12}O_{19}$ coating with a higher strain tolerance and relieve thermal stresses which may induce interface crack growth and coating spallation. This would be consistent with the present study where $SrAl_{12}O_{19}$ well bonds with YSZ layer even after long-term thermal cycling.

As shown in Figure 8D, the new ceramic topcoat $SrAl_{12}O_{19}$ investigated here shows a relative shorter thermal cycling lifetime than the standard YSZ coating when it was applied as single layers. How, it can be comparable to LMA coating and much better than other new TBCs such as $Gd_2Zr_2O_7$. The $SrAl_{12}O_{19}$/YSZ DCL coating exhibits much longer lifetime than the relevant single-layer coating, and also shows improved performance in comparison with YSZ coatings. It should be noted that the current results are based on cyclic furnace tests, while actual engine operation involves a temperature gradient. In the $SrAl_{12}O_{19}$/YSZ DCL coatings, $SrAl_{12}O_{19}$ layer with high phase stability and sintering resistance can withstand higher temperature and act as a thermal insulator to protect the inner YSZ layer. Therefore, it seems that the beneficial aspects of the $SrAl_{12}O_{19}$/YSZ DCL coatings might become even more significant in higher temperature test with extreme thermal gradients. Further work is in progress to prepare $SrAl_{12}O_{19}$-based T/EBCs on ceramic matrix composite substrates and the performance will be evaluated by using a burner rig test facility.

4 | CONCLUSIONS

The present study examines $SrAl_{12}O_{19}$ as potential TBC materials that may overcome the limitations of conventional YSZ and $LaMgAl_{11}O_{19}$. The results show that $SrAl_{12}O_{19}$ coating can be deposited by atmospheric

plasma spraying without a change in chemistry. After thermal cycling or long-term aging at 1300°C, $SrAl_{12}O_{19}$ coating still keeps the magnetoplumbite structure. $SrAl_{12}O_{19}$ coating exhibits large concentrations of cracks and pores (~26% porosity) after 1000 hours heat treatment at 1300°C, which is highly desirable for TBC applications. In contrast, the total porosity of YSZ coatings progressively decreases from the initial value of ~18% to ~5%. Due to the contribution of porous microstructure, an ultralow thermal conductivity (~1.36 W m^{-1} K^{-1}) can be maintained for $SrAl_{12}O_{19}$ coating even after 1000 hours aging at 1300°C, which is far lower than that of the YSZ coating (~1.98 W m^{-1} K^{-1}). In thermal cyclic fatigue test, spallation at the outer rim is observed for $SrAl_{12}O_{19}$ coating after 163 cycles, which is mainly a result of thermal expansion mismatch between $SrAl_{12}O_{19}$ coating and bond coat. By using an YSZ buffer layer, the thermal cycling durability has been largely improved. The $SrAl_{12}O_{19}$/YSZ DCL TBC undertakes a cyclic lifetime of ~512 cycles, which is not only much longer than that of YSZ coating (~392 cycles), but also can be comparable to $LaMgAl_{11}O_{19}$/YSZ coating (~574 cycles). Considering the outstanding thermophysical properties and structure stability, $SrAl_{12}O_{19}$ might be promising TBC candidate for next generation gas turbine.

ACKNOWLEDGMENTS

This work was financially supported by the National Natural Science Foundation of China (No. 51702244), and National Science and Technology Major Project (2017-VI-0010-0081). Wenjia Song acknowledges the support of the "Freigeist" Fellowship of the VolkswagenStiftung for "Volcanic Ash Deposition in Jet Engines" (VADJEs, No 89705). We are also grateful to Jianing Jiang and Longhui Deng from Wuhan University of Technology for producing thermal barrier coatings.

CONFLICTS OF INTEREST

There are no conflicts to declare.

ORCID

Xin Zhou https://orcid.org/0000-0002-6148-3347

REFERENCES

1. Perepezko JH. The hotter the engine, the better. Science. 2009;326:1068–9. https://doi.org/10.1126/science.1179327
2. Padture NP. Advanced structural ceramics in aerospace propulsion. Nat Mater. 2016;15:804–9. https://doi.org/10.1038/nmat4687
3. Padture NP, Gell M, Jordan EH. Thermal barrier coatings for gas-turbine engine applications. Science. 2002;296:280–4. https://doi.org/10.1126/science.1068609
4. Clarke DR, Oechsner M, Padture NP. Thermal-barrier coatings for more efficient gas-turbine engines. MRS Bull. 2012;37:891–8. https://doi.org/10.1557/mrs.2012.232
5. Padture NP. Environmental degradation of high-temperature protective coatings for ceramic-matrix composites in gas-turbine engines. npj Mater Degrad. 2019;3:1–6. https://doi.org/10.1038/s41529-019-0075-4
6. Lee KN, Fox DS, Eldridge JI, Zhu D, Robinson RC, Bansal NP, et al. Upper temperature limit of environmental barrier coatings based on mullite and BSAS. J Am Ceram Soc. 2003;86:1299–306. https://doi.org/10.1111/j.1151-2916.2003.tb03466.x
7. Lee KN, Fox DS, Bansal NP. Rare earth silicate environmental barrier coatings for SiC/SiC composites and Si_3N_4 ceramics. J Eur Ceram Soc. 2005;25:1705–15. https://doi.org/10.1016/j.jeurceramsoc.2004.12.013
8. Zhu D, Miller R. Thermal and environmental barrier coatings for advanced propulsion engine systems. Washington, DC: NASA; 2004. NASA/TM-2004-213129.
9. Turcer LR, Padture NP. Towards multifunctional thermal environmental barrier coatings (TEBCs) based on rare-earth pyrosilicate solid-solution ceramics. Scr Mater. 2018;154:111–7. https://doi.org/10.1016/j.scriptamat.2018.05.032
10. Tian Z, Lin C, Zheng L, Sun L, Li J, Wang J. Defect-mediated multiple-enhancement of phonon scattering and decrement of thermal conductivity in $(Y_xYb_{1-x})_2SiO_5$ solid solution. Acta Mater. 2018;144:292–304. https://doi.org/10.1016/j.actamat.2017.10.064
11. Krause AR, Garces HF, Herrmann CE, Padture NP. Resistance of $2ZrO_2 \cdot Y_2O_3$ top coat in thermal/environmental barrier coatings to calcia-magnesia-aluminosilicate attack at 1500° C. J Am Ceram Soc. 2017;100:3175–87. https://doi.org/10.1111/jace.14854
12. Tian Z, Zheng L, Hu W, Sun L, Zhang J, Wang J. Tunable properties of $(Ho_xY_{1-x})_2SiO_5$ as damage self-monitoring environmental/thermal barrier coating candidates. Sci Rep-UK. 2019;9:415. https://doi.org/10.1038/s41598-018-36883-2
13. Xu J, Sarin V, Dixit S, Basu S. Stability of interfaces in hybrid EBC/TBC coatings for Si-based ceramics in corrosive environments. Int J Refract Met H. 2015;49:339–49. https://doi.org/10.1016/j.ijrmhm.2014.08.013
14. Cao X, Vassen R, Stoever D. Ceramic materials for thermal barrier coatings. J Eur Ceram Soc. 2004;24:1–10. https://doi.org/10.1016/S0955-2219(03)00129-8
15. Lu MH, Xiang HM, Feng ZH, Wang XY, Zhou YC. Mechanical and thermal properties of Yb_2SiO_5: a promising material for T/EBC s applications. J Am Ceram Soc. 2016;99:1404–11. https://doi.org/10.1111/jace.14085
16. Zhou X, Chen T, Yuan JY, Deng ZH, Zhang H, Jiang JN, et al. Failure of plasma sprayed nano-zirconia-based thermal barrier coatings exposed to molten CaO-MgO-Al_2O_3-SiO_2 deposits. J Am Ceram Soc. 2019;102:6357–71. https://doi.org/10.1111/jace.16498
17. Lipkin DM, Krogstad JA, Gao Y, Johnson CA, Nelson WA, Levi CG. Phase evolution upon aging of air-plasma sprayed t′-Zirconia Coatings: I—synchrotron X-Ray diffraction. J Am Ceram Soc. 2013;96:290–8. https://doi.org/10.1111/j.1551-2916.2012.05451.x
18. Schulz U. Phase transformation in EB-PVD yttria partially stabilized zirconia thermal barrier coatings during annealing. J Am Ceram Soc. 2000;83:904–10. https://doi.org/10.1111/j.1151-2916.2000.tb01292.x
19. Cipitria A, Golosnoy I, Clyne T. A sintering model for plasma-sprayed zirconia TBCs. Part I: free-standing coatings. Acta Mater. 2009;57:980–92.
20. Pan W, Phillpot SR, Wan C, Chernatynskiy A, Qu Z. Low thermal conductivity oxides. MRS Bull. 2012;37:917–22. https://doi.org/10.1557/mrs.2012.234

21. Vassen R, Cao X, Tietz F, Basu D, Stöver D. Zirconates as new materials for thermal barrier coatings. J Am Ceram Soc. 2000;83:2023–8. https://doi.org/10.1111/j.1151-2916.2000.tb01506.x
22. Wu J, Wei X, Padture NP, Klemens PG, Gell M, García E, et al. Low-thermal-conductivity rare-earth zirconates for potential thermal-barrier-coating applications. J Am Ceram Soc. 2002;85:3031–5. https://doi.org/10.1111/j.1151-2916.2002.tb00574.x
23. Munawar AU, Schulz U, Cerri G, Lau H. Microstructure and cyclic lifetime of Gd and Dy-containing EB-PVD TBCs deposited as single and double-layer on various bond coats. Surf Coat Technol. 2014;245:92–101. https://doi.org/10.1016/j.surfcoat.2014.02.047
24. Guo L, Guo H, Peng H, Gong S. Thermophysical properties of Yb_2O_3 doped $Gd_2Zr_2O_7$ and thermal cycling durability of $(Gd_{0.9}Yb_{0.1})_2Zr_2O_7$/YSZ thermal barrier coatings. J Eur Ceram Soc. 2014;34(5):1255–1263. https://doi.org/10.1016/j.jeurceramsoc.2013.11.035
25. Chen H, Liu Y, Gao Y, Tao S, Luo H. Design, preparation, and characterization of graded YSZ/$La_2Zr_2O_7$ thermal barrier coatings. J Am Ceram Soc. 2010;93:1732–40. https://doi.org/10.1111/j.1551-2916.2010.03610.x
26. Zhong X, Zhao H, Zhou X, Liu C, Wang L, Shao F, et al. Thermal shock behavior of toughened gadolinium zirconate/YSZ double-ceramic-layered thermal barrier coating. J Alloy Compd. 2014;593:50–5.
27. Zhu D, Bansal NP, Miller RA. Thermal conductivity and stability of HfO_2-Y_2O_3 and $La_2Zr_2O_7$ evaluated for 1650°C thermal/environmental barrier coating applications. Washington, DC: NASA; 2003. NASA/TM-2003-212544.
28. Latzel S, Vaßen R, Stöver D. New environmental barrier coating system on carbon-fiber reinforced silicon carbide composites. J therm Spray Techn. 2005;14:268–72. https://doi.org/10.1361/10599630523854
29. Poerschke DL, Sluytman JS, Wong K, Levi CG. Thermochemical compatibility of ytterbia–(hafnia/silica) multilayers for environmental barrier coatings. Acta Mater. 2013;61:6743–55. https://doi.org/10.1016/j.actamat.2013.07.047
30. Poerschke DL, Hass DD, Eustis S, Seward GGE, Van Sluytman JS, Levi CG. Stability and CMAS resistance of ytterbium-silicate/hafnate EBCs/TBC for SiC composites. J Am Ceram Soc. 2015;98:278–86. https://doi.org/10.1111/jace.13262
31. Winter MR, Clarke DR. Oxide materials with low thermal conductivity. J Am Ceram Soc. 2007;90:533–40. https://doi.org/10.1111/j.1551-2916.2006.01410.x
32. Zou B, Khan ZS, Gu L, Fan X, Huang W, Wang Y, et al. Microstructure, oxidation protection and failure mechanism of Yb_2SiO_5/$LaMgAl_{11}O_{19}$ coating deposited on C/SiC composites by atmospheric plasma spraying. Corros Sci. 2012;62:192–200. https://doi.org/10.1016/j.corsci.2012.05.020
33. Vaßen R, Jarligo MO, Steinke T, Mack DE, Stöver D. Overview on advanced thermal barrier coatings. Surf Coat Technol. 2010;205:938–42.
34. Gadow R, Lischka M. Lanthanum hexaaluminate—novel thermal barrier coatings for gas turbine applications—materials and process development. Surf Coat Technol. 2002;151:392–9. https://doi.org/10.1016/S0257-8972(01)01642-5
35. Bansal NP, Zhu D. Thermal properties of oxides with magnetoplumbite structure for advanced thermal barrier coatings. Surf Coat Technol. 2008;202:2698–703. https://doi.org/10.1016/j.surfcoat.2007.09.048
36. Sun J, Wang J, Zhou X, Hui YU, Dong S, Li L, et al. Thermal cycling behavior of the plasma-sprayed coating of lanthanum hexaaluminate. J Eur Ceram Soc. 2018;38:1919–29. https://doi.org/10.1016/j.jeurceramsoc.2017.12.046
37. Chen X, Gu L, Zou B, Wang Y, Cao X. New functionally graded thermal barrier coating system based on $LaMgAl_{11}O_{19}$/YSZ prepared by air plasma spraying. Surf Coat Technol. 2012;206:2265–74. https://doi.org/10.1016/j.surfcoat.2011.09.076
38. Zou B, Hui YU, Huang W, Zhao S, Chen X, Xu J, et al. Oxidation protection of carbon/carbon composites with a plasma-sprayed ZrB_2–SiC–Si/Yb_2SiO_5/$LaMgAl_{11}O_{19}$ coating during thermal cycling. J Eur Ceram Soc. 2015;35:2017–25. https://doi.org/10.1016/j.jeurceramsoc.2015.01.015
39. Chen X, Zhao YU, Huang W, Ma H, Zou B, Wang Y, et al. Thermal aging behavior of plasma sprayed $LaMgAl_{11}O_{19}$ thermal barrier coating. J Eur Ceram Soc. 2011;31:2285–94. https://doi.org/10.1016/j.jeurceramsoc.2011.05.036
40. Zhu D, Fox DS, Bansal NP, Miller RA. Advanced oxide material systems for 1650°C thermal/environmental barrier coating applications. Washington, DC: NASA; 2004. NASA/TM-2004-213219.
41. Wang CA, Lu H, Huang Z, Xie H. Enhanced anti-deliquescent property and ultralow thermal conductivity of magnetoplumbite-type $LnMeAl_{11}O_{19}$ materials for thermal barrier coating. J Am Ceram Soc. 2018;101:1095–104. https://doi.org/10.1111/jace.15285
42. Dong S, Song B, Zhou GS, Hansz B, Liao HL, Coddet C. Multilayered thermal barrier coatings fabricated by plasma-spraying and dry-ice blasting: microstructure characterization and prolonged lifetime. Surf Coat Technol. 2013;236:557–67. https://doi.org/10.1016/j.surfcoat.2013.10.066
43. Xie X, Guo H, Gong S, Xu H. Lanthanum–titanium–aluminum oxide: a novel thermal barrier coating material for applications at 1300°C. J Eur Ceram Soc. 2011;31:1677–83. https://doi.org/10.1016/j.jeurceramsoc.2011.03.036
44. Ma W, Mack D, Malzbender J, Vaßen R, Stöver D. Yb_2O_3 and Gd_2O_3 doped strontium zirconate for thermal barrier coatings. J Eur Ceram Soc. 2008;28:3071–81. https://doi.org/10.1016/j.jeurceramsoc.2008.05.013
45. Li G, Xie H, Yang G, Liu G, Li C, Li C. A comprehensive sintering mechanism for TBCs-Part I: an overall evolution with two-stage kinetics. J Am Ceram Soc. 2017;100:2176–89. https://doi.org/10.1111/jace.14784
46. Li G, Wang L, Yang G. A novel composite-layered coating enabling self-enhancing thermal barrier performance. Scr Mater. 2019;163:142–7. https://doi.org/10.1016/j.scriptamat.2019.01.010
47. Ren X, Zhao M, Wan C, Zheng Y, Pan W. High-temperature aging of plasma sprayed quasi-eutectoid $LaYbZr_2O_7$–Part II: microstructure & thermal conductivity. J Am Ceram Soc. 2015;98:2836–42. https://doi.org/10.1111/jace.13673
48. Li G, Xie H, Yang G, Liu G, Li C, Li C. A comprehensive sintering mechanism for TBCs-Part II: multiscale multipoint interconnection-enhanced initial kinetics. J Am Ceram Soc. 2017;100:4240–51. https://doi.org/10.1111/jace.14940
49. Li G, Yang G, Li C, Li C. A comprehensive sintering mechanism for thermal barrier coatings-Part III: substrate constraint effect on healing of 2D pores. J Am Ceram Soc. 2018;101:3636–48. https://doi.org/10.1111/jace.15501
50. Li G, Yang G. Understanding of degradation-resistant behavior of nanostructured thermal barrier coatings with bimodal structure. J Mater Sci Technol. 2019;35(3):231–8. https://doi.org/10.1016/j.jmst.2018.09.054

51. Girolamo GD, Blasi C, Pagnotta L, Schioppa M. Phase evolution and thermophysical properties of plasma sprayed thick zirconia coatings after annealing. Ceram Int. 2010;36:2273–80.
52. Evans AG, Mumm D, Hutchinson J, Meier G, Pettit F. Mechanisms controlling the durability of thermal barrier coatings. Prog Mater Sci. 2001;46:505–53. https://doi.org/10.1016/S0079-6425(00)00020-7

How to cite this article: Zhou X, Song W, Yuan J, et al. Thermophysical properties and cyclic lifetime of plasma sprayed $SrAl_{12}O_{19}$ for thermal barrier coating applications. *J Am Ceram Soc*. 2020;00:1–13. https://doi.org/10.1111/jace.17319

SUPPORTING INFORMATION

Additional supporting information may be found online in the Supporting Information section.